NACA RM L57F19

RESEARCH MEMORANDUM

FREE-FLIGHT INVESTIGATION OF JET EFFECTS AT LOW SUPERSONIC

MACH NUMBERS ON A FIGHTER-TYPE CONFIGURATION

EMPLOYING A TAIL-BOOM ASSEMBLY

LONGITUDINAL STABILITY AND TRIM

By Bruce G. Jackson and Norman L. Crabill

Langley Aeronautical Laboratory
Langley Field, Va.

CLASSIFIED DOCUMENT

NATIONAL ADVISORY COMMITTEE
FOR AERONAUTICS
WASHINGTON
August 30, 1957

NATIONAL ADVISORY COMMITTEE FOR AERONAUTICS

RESEARCH MEMORANDUM

FREE-FLIGHT INVESTIGATION OF JET EFFECTS AT LOW SUPERSONIC

MACH NUMBERS ON A FIGHTER-TYPE CONFIGURATION

EMPLOYING A TAIL-BOOM ASSEMBLY

LONGITUDINAL STABILITY AND TRIM

By Bruce G. Jackson and Norman L. Crabill

SUMMARY

Flight tests have been made over a Mach number range of 1.1 to 1.4 to study the effects of a simulated afterburning turbojet engine on the gross longitudinal flight characteristics of two geometrically identical models of a swept-wing fighter-type configuration. The tail surfaces were mounted on a relatively large tail boom of rectangular cross section extending aft of and above the jet exit. The tests were made with the aid of the free-flight rocket-boosted model technique, solid-propellant rocket motors were used to simulate turbojet engines, and pulse rockets were used to disturb the models in flight.

The effects of power were to decrease the trim normal-force coefficient by 0.09 and to decrease the trim angle of attack by 1.8°. The normal-force coefficient at a constant angle of attack was increased while the pitching-moment coefficient at a constant angle of attack was decreased. There were no apparent power effects on the lift-curve slope except possibly at higher Mach numbers. Any differences between power on and power off noted on the pitching-moment-curve slope and aerodynamic-center location fall within the accuracy of the data.

INTRODUCTION

A number of recent airplanes, such as the McDonnell F3H, McDonnell F-101, and Douglas X-3, have utilized the tail-boom approach in an attempt to solve the conflicting problems of stability and loss of engine efficiency due to long tail pipes. Some other airplanes, such as the

McDonnell F2H, Grumman F9F and MIG-15, having more conventional fuselages, allow the jet exhaust to pass under the horizontal-tail surfaces. Even if the direct thrust moment be negligibly small, important problems of trim, stability, control, and many structural problems such as the effects of heat, fatigue due to jet exhaust noise, and boom and tail-surface flexibility have arisen in such installations. Because of a lack of sufficient information on such interference effects, a limited research program has been conducted by the Pilotless Aircraft Research Division of the Langley Aeronautical Laboratory. The purpose of this program was to investigate the effects of a simulated afterburning turbojet engine on the stability characteristics of a model of a swept-wing fighter-type configuration having a relatively large tail-boom assembly. This paper presents a study of the gross jet effects on the longitudinal flight characteristics of two models having the same configuration.

SYMBOLS

Figure 1 presents the body-axis system with the positive displacements, forces, and moments indicated by the arrows.

A   area of jet exit, sq ft

a   linear acceleration, ft/sec^2

b   span, ft

$\bar{c}$ wing mean aerodynamic chord, ft

C_X axial force coefficient, $\dfrac{a_X}{g}\dfrac{W}{q_\infty S}$

C_D drag coefficient, $-C_X \cos\alpha + C_N \sin\alpha$

C_L lift coefficient, $C_N \cos\alpha + C_X \sin\alpha$

C_m pitching-moment coefficient about center of gravity, $\dfrac{\ddot{\theta} I_Y}{q_\infty S \bar{c}}$

C_N normal-force coefficient, $\dfrac{a_Z}{g}\dfrac{W}{q_\infty S}$

C_F thrust-force coefficient, $\dfrac{\text{Thrust force}}{q_\infty A}$

C_Y side-force coefficient, $\dfrac{a_Y}{g}\dfrac{W}{q_\infty S}$

g	gravitational acceleration, ft/sec^2
I	mass moment of inertia about center of gravity, slug-ft^2
M	Mach number
p	free-stream static pressure, lb/sq in.
p_j	jet static pressure, lb/sq in. abs
p_j	jet total pressure, lb/sq in. abs
q_∞	dynamic pressure, lb/sq ft
r	radius, ft
R	Reynolds number
S	total wing area, sq ft
t	time, sec
V	velocity, ft/sec
W	weight of model, lb
X	distance parallel to X-axis, ft
Y	distance parallel to Y-axis, ft
Z	distance parallel to Z-axis, ft
α	angle of attack, deg
γ	flight-path angle, deg
θ	angle of pitch, deg
$\ddot{\theta}$	pitching angular acceleration, radians/sec^2
$\dfrac{\theta}{L}$	wing influence coefficient, radians/lb
ψ	direction toward which wind blows, deg from true North
η	spanwise station, $\dfrac{Y}{b/2}$, percent semispan

C_{m_α} static stability parameter, $\dfrac{dC_m}{d\alpha}$

$C_{m_{C_N}}$ static stability parameter, $\dfrac{dC_m}{dC_N}$

$C_{m_q} + C_{m_{\dot\alpha}}$ longitudinal rotary damping derivative,

$$57.3 \left[\frac{dC_m}{d\left(\dfrac{d\theta/dt \ \bar{c}}{2V}\right)} + \frac{dC_m}{d\left(\dfrac{d\alpha/dt \ \bar{c}}{2V}\right)} \right]$$

C_{N_α} lift-curve slope, $\dfrac{dC_N}{d\alpha}$

Subscripts:

ac   aerodynamic center

cg   center of gravity

e   elastic

r   rigid

t   trim condition

X   with respect to X-axis

Y   with respect to Y-axis

Z   with respect to Z-axis

The symbol Δ preceding a symbol indicates increment due to power unless otherwise defined.

MODELS

Airframe

A three-view drawing of the configuration tested is given in figure 2(a). Photographs of the models are presented in figures 2(b) and 2(c). The physical characteristics of the models are presented in table I. The sonic area rule was incorporated into the body design, and the normal area distribution is given in figure 3. Body ordinates are given in table II.

The nose sections of the models were constructed of aluminum alloy. The body sections were made up of a steel rocket-motor housing for model I and a magnesium-alloy rocket-motor housing for model II, each surrounded by laminated mahogany which was faired to the designed body contour. The swept wings and tail surfaces were of solid-aluminum construction. The primary structure of the tail boom of model I was wood, whereas for model II it was metal.

Turbojet Simulator

A 5-inch solid-propellant Cordite rocket motor, modified after the method of reference 1, was used as a turbojet simulator. This rocket motor approximately simulated present-day turbojet engines operating with afterburner at a Mach number of 1.2 at an altitude of 35,000 feet for a model test Mach number of 1.2 at an altitude of 3,000 feet. It was found from static ground firings conducted at the Langley rocket test cell that, with a jet-exit diameter of 3.415 inches a sonic exit was obtained and the desired simulator parameters could most nearly be approximated. Figure 4(a) presents a cutaway drawing of the model exposing the rocket-motor installation and its pertinent parts. Operating characteristics obtained from the static ground firings of the simulator are included in figure 4(a). Figure 4(b) is a photograph of the jet exit. The center line of the simulator coincided with the model reference line and passed within ±0.02 inch of the model center of gravity.

INSTRUMENTATION

An NACA telemeter transmitter relayed continuous signals from the instruments contained in each model to a ground receiving station. The transmitted information obtained from both models included:

Flow direction at the nose in the pitch plane

Normal acceleration at the nose

Normal acceleration at the center of gravity

Transverse acceleration at the center of gravity

Longitudinal acceleration at the center of gravity

Flow-direction-indicator base pressure

Free-stream stagnation pressure

An NACA modified SCR-584 tracking radar and a CW Doppler veloci-
meter were used to obtain the model's instantaneous position in space and
velocity throughout the flight-test range. Atmospheric conditions were
measured by means of a rawinsonde released shortly after the flight time.

TESTS

Preflight Structural Tests

Presented in figure 5 are the wing structural influence coefficients
for 25- and 50-percent-chord loadings obtained from static loading tests.
Vibration tests were made and the resulting nodal lines and their corre-
sponding resonant frequencies are shown in figure 6. The difference in
the resonant frequencies for wing first bending encountered on the two
models (model I - 34.5 cycles per second and model II - 55 cycles per
second) is believed to have resulted from the differences in the distri-
butions of the mass and elasticity in the two fuselages.

Flight Tests

Flight tests were conducted at the Langley Pilotless Aircraft
Research Station at Wallops Island, Va. Each model was boosted from the
ground to flight test velocity and altitude with a 6-inch ABL Deacon
rocket motor. The Mach number attained at booster burnout was approxi-
mately 1.2. The model then separated from the booster due to the differ-
ences in drag-weight ratios between the model and the model-booster combi-
nation. After a delay, the sustainer rocket-motor ignited and accelerated
the model to its maximum Mach number. In the case of model I, because of
a long delay due to starting difficulties, the maximum Mach number
attained was 1.34. Model II, which functioned properly, reached a peak
Mach number of 1.40.

The models were disturbed in pitch while in flight by four pulse
rockets located in the nose. Disturbances in pitch were also encountered
(1) upon separation of the model from the booster (2) upon simulator igni-
tion and (3) upon simulator burnout, because of the abrupt trim change
arising from the sudden power changes. The atmospheric conditions are
summarized in figure 7. It is evident from these data that the flight of
model I took place in air having a temperature lapse rate approximately
half way between the dry and wet adiabats and that appreciable heating
of the surface of the earth had occurred by the time of the flight. Only
scattered clouds were present at the time, and the wind direction was
such as to transport any turbulence originating over the land to the test
area over the water. Reference 2 indicates a correlation between such

atmospheric conditions and the occurrence of atmospheric turbulence at the location of these tests. The atmospheric conditions existing during the test of model II however were more complex. Although the same marginal lapse rate was encountered at various altitudes, the initial temperature inversion and the haze existing at the time of the test indicated little or no ground heating. In spite of high wind velocity, its direction was parallel to the shore line. Thus it is probable that the flight of the second model occurred in relatively smooth air.

The test conditions are summarized in figure 8. Reynolds number and dynamic pressure are presented in figures 8(a) and (b) as a function of Mach number. Ratio of estimated jet total pressure to free-stream static pressure and estimated thrust coefficient are plotted as a function of Mach number in figures 8(c) and (d). These estimates are based on the data obtained from the ground test of the simulator.

CORRECTIONS AND ACCURACIES

Instrument misalinement and displacement corrections were made where necessary. Table III(a) presents the estimated probable errors in the basic data, and the calculated effect on the longitudinal stability derivatives is presented in table III(b).

ANALYSIS

The body-axis system shown in figure 1 was used for the analysis. The analysis was conducted on the transient motions of the model resulting from the disturbances of the model in pitch. The longitudinal stability analysis conducted on these oscillations is based on the usual assumption of two degrees of freedom in pitch. A more detailed discussion of the methods used in reducing the data from flight time histories and the assumptions made in and the limitations of the test technique can be found in references 3 and 4.

A short discussion of the theory that is compared with the experimental stability data is given in the appendix.

RESULTS AND DISCUSSION

Presented in figure 9 are time histories of the basic quantities for both models. During the power-on portion of the flight the indicated drag coefficient shown dashed in figure 9 is not a true drag coefficient

because it includes the thrust component of the simulator which resulted in longitudinal accelerations that exceeded the instrument range. It is presented because it gives an accurate indication of when the power changes occurred. Although oscillations in sideslip were evident it should be noted that the model trimmed with essentially zero side force. Reynolds numbers based on wing mean aerodynamic chord ranged from a minimum of 9×10^6 to a maximum of 11.6×10^6.

Trim Characteristics

The most significant jet effect encountered in this test was the change in trim due to power. Trim normal-force coefficient and trim angle-of-attack data are presented in figure 10. The increment in trim normal-force coefficient due to the application of power is presented in figure 10(c). The measured increments for the flexible case are shown by the solid lines; these flexible increments have been corrected for aeroelasticity and are shown as the dashed lines. The resulting increment in C_{N_t} due to jet effects for the rigid case is seen to be about -0.09. Results from reference 5 at Mach number of 1.3 show a value of ΔC_{N_t} of -0.18 for a configuration with a supersonic exit and a horizontal stabilizer near the jet exit, and results from reference 6 at a Mach number of 1.5 show a value of ΔC_{N_t} of -0.07 for a configuration with a sonic exit and a high horizontal tail mounted on the vertical fin. Each of the reference configurations employed a tail boom but had differing stability, tail effectiveness, and differences in shape and fairing between the boom and body. (See ref. 7.) There is no direct way to correlate the results of the reference data with the data of this test because of the many variables involved. However, they all show the same trend of decreasing the trim normal-force coefficient with the greatest decrease for the horizontal tail nearest the jet exit.

The trim angle-of-attack increment due to the application of power is presented in figure 10(f). Flexible and rigid data are shown with an increment in rigid α_t of $-1.8°$ due to power.

It is believed there was a shift in the angle-of-attack indication of model I of approximately $1°$ throughout the entire flight. Unpublished angle-of-attack data of an identical configuration show close agreement with model II. This shift is not important for the present purposes since power effects are the prime objective of this report and it has no effect on the slopes and power increments.

The differences in trim due to power effects between models I and II (fig. 10(f)) may be due to small unintentional differences in the jet-exit fairing and to the effect of the heat from the sustainer motor on the

metal skeleton of the boom of model II. (The boom of model I was
essentially all wood.) These trim differences are, however, of the same
order of magnitude as the estimated probable errors.

Lift

Basic lift plots of C_N against α are presented in figure 11.
In the lower plot for model I in figure 11 the effect of the power change
can be noted; data points are plotted through the transition from power
on to power off. Since, during the power-on portion of this oscillation,
data were available over only one-half cycle, the fairing of these points
must be viewed with caution.

Lift-curve slopes obtained from plots of C_N against α in
figure 11 are presented in figure 12(a) as plain symbols. The faired
curve represents the calculated theoretical flexible lift-curve slope.
In figure 12(b) rigid lift-curve slopes are shown in which calculated
flexibility increments were added to the flexible data of figure 12(a).
Good agreement is noted in the comparison of the experimental data of each
model with the calculated theoretical curves. There appears to be a pos-
sible decrease in lift-curve slope due to power at the highest Mach num-
ber. Some power effects may possibly have been masked by the flexibility
corrections. Reference 6 shows a possible slight increase in lift-curve
slope at a Mach number of 1.5. A more extensive investigation should be
conducted before any concrete conclusions are made concerning power
effects on lift-curve slope.

In figure 12(c), C_N at $\alpha = 2^\circ$ is presented as a function of Mach
number. An angle of attack of 2° was used as it is a value common to all
oscillations. The effect of power on C_N at $\alpha = 2^\circ$ as determined from
the data of both models was an increase of 0.03 from M = 1.20 to 1.33.
When based on the total plan-form area of the exposed horizontal tail and
the boom aft of the jet exit, this increment of 0.030 becomes 0.137.

Pitching Moment

No direct thrust moments were encountered since the sustainer motor
center line (thrust axis) passed within ±0.02 inch of the model center of
gravity.

Basic plots of C_m against α are presented in figure 13. Again,
in the lower plot for model I, the effects of power can be seen; data
points are plotted through the transition from power on to power off.
Since, during the power-on portion of this oscillation, data were avail-
able over only one-half cycle, the fairing of these points must be viewed
with caution.

Pitching-moment-curve slope C_{m_α} as obtained from the basic plots of figure 13, is presented in figure 14(a) plotted as a function of Mach number and represented by the plain symbols. The faired curve for both models is identical and shows consistent results for the two models. The flagged symbols in figure 14(a), model II, represents C_{m_α} as computed from the period obtained from the transient motions. The periods for the two data points shown were considered to be the only ones valid for computing C_{m_α}. The remaining oscillations contained sufficient cross coupling to prevent an accurate computation of C_{m_α} by this method. There are no apparent power effects on C_{m_α}. In figure 14(b) the measured aerodynamic-center location $\frac{X_{ac}}{\bar{c}}$ plotted against Mach number is presented. The plain symbols represent $\frac{X_{ac}}{\bar{c}}$ as determined from plots of C_m against C_N. The faired curve is the calculated theoretical flexible $\frac{X_{ac}}{\bar{c}}$. Figure 14(c) shows the rigid $\frac{X_{ac}}{\bar{c}}$ determined from the flexible $\frac{X_{ac}}{\bar{c}}$ of figure 14(b) plus a calculated flexibility increment. The dashed curve represents the calculated rigid $\frac{X_{ac}}{\bar{c}}$. Good agreement is noted between the aerodynamic-center location of model I and model II with the calculated curve. Any power effects on the aerodynamic-center location are evidently as small as the accuracy with which this quantity can be measured.

In figure 14(d) pitching-moment coefficient C_m at $\alpha = 2°$ plotted against Mach number is presented. An angle of attack of $2°$ was used for the same reason as in the lift analysis. The effects of power on C_m at $\alpha = 2°$ plotted against Mach number are shown in figure 14(e). Power on produced a change in C_m at $\alpha = 2°$ of -0.048 on both models from $M = 1.20$ to 1.33. If the interference effects of the jet are assumed to act at the aerodynamic center of the horizontal tail, an increment in C_N at $\alpha = 2°$ (based on wing area) due to power of 0.025 can be computed from the ΔC_m at $\alpha = 2°$ of -0.048. When this increment of 0.025 is based on total projected area aft of the jet exit, it becomes 0.114 which compares well with the measured increment of 0.137 which is based on the same area.

Dynamic Stability

All the transient motions of model I and two of those of model II exhibited irregularities in period and damping which precluded any

dynamic analysis. These irregularities can be observed in the time
histories presented in figure 9. Since it was believed that model I
flew in turbulent air (see discussion on page 6), the irregularities of
model I were probably due to the response of the model to atmospheric tur-
bulence and were aggravated by some longitudinal-lateral coupling effects.
Model II irregularities were believed to be due to longitudinal-lateral
coupling since the flight was in comparatively smooth air. However, two
of the transients were relatively free from the effects of longitudinal-
lateral coupling and were analyzed for dynamic stability data which are
presented in figure 15.

Shown in figure 15(a) are the period and time for the transient
motions to damp to one-half amplitude. Figure 15(b) is a plot of the
longitudinal rotary damping derivative $C_{m_q} + C_{m_{\dot{a}}}$ against Mach number.

The circular symbols represent the measured flexible data. The diamond
symbols are the measured data corrected to rigid-wing downwash. The solid
line is the calculated $C_{m_q} + C_{m_{\dot{\alpha}}}$ of the tail alone, based on rigid-wing
downwash. As no power-on data are available, no power effects on
$C_{m_q} + C_{m_{\dot{\alpha}}}$ are presented.

Drag

Power-off drag data are presented in figure 16 as basic plots of
drag coefficient against normal-force coefficient. The range over which
the data were obtained makes it difficult to determine accurately the
minimum drag coefficient and the induced drag coefficient. Because of
the lack of thrust data during flight, no power-on drag data were
obtained; therefore, no power effects on drag are presented.

CONCLUSIONS

Two geometrically identical models of a swept-wing fighter-type
configuration having swept tail surfaces mounted on a relatively large
tail boom aft of and above the jet exit have been free-flight tested by
the Langley Pilotless Aircraft Research Division to determine the jet
effects on longitudinal stability and trim. From the results obtained
from this test the following conclusions may be drawn:

1. The effect of power was to decrease the trim normal-force coeffi-
cient by approximately 0.09 and to decrease the trim angle of attack by
approximately 1.8°.

2. There were no apparent power effects on lift-curve slope except possibly at the highest Mach number.

3. Any apparent power effects noted on the pitching-moment-curve slope and aerodynamic-center location fall within the accuracy of the data.

Langley Aeronautical Laboratory,
    National Advisory Committee for Aeronautics,
        Langley Field, Va., June 6, 1957.

APPENDIX

AERODYNAMIC THEORY WITH AEROELASTIC CONSIDERATIONS

Chordwise and spanwise distributions of angle-of-attack-induced wing and body loads were determined by a form of slender-wing-body theory. Modifications applied to Spreiter's slender-wing-body theory (ref. 8) were the "width" correction for a wing whose leading edge is near the vertex Mach cone proposed by Nielsen, Katzen, and Tang (ref. 9), and simple approximations to the tip and trailing-edge corrections given by Cohen for wings alone (ref. 10). In addition, the body lift was assumed swept back along Mach lines.

Downwash over the tail was computed by the method of Mirels and Haefeli (ref. 11). The nose lift and aerodynamic-center location were also obtained from slender-body theory.

An aeroelastic analysis similar to that described by Vitale (ref. 12) was used. However, the section lift force was assumed to be acting at the chordwise location of the local aerodynamic center defined by the theory outlined above and not at an arbitrarily assumed 25 or 50 percent of local chord as suggested in reference 12. Structural influence coefficients appropriate to this aerodynamic-center location at each Mach number were then used. Also, the forward shift in wing aerodynamic center due to wing aeroelasticity was assumed to occur along the line joining the section aerodynamic centers.

The effect of wing aeroelasticity on the downwash over the tail was computed by Percy J. Bobbitt of the Langley Stability Research Division for $M = 1.377$ by using 20 rectangular horseshoe vortices to approximate the spanwise and trailing vorticity distributions. The ratio $\epsilon_{\alpha_e}/\epsilon_{\alpha_r}$ so obtained was assumed to vary linearly with the quantity $qC_{L_{\alpha_r}}$ in obtaining flexible downwash at other Mach numbers and dynamic pressures.

The effect of horizontal-tail aeroelasticity was negligible.

REFERENCES

1. De Moraes, Carlos A., Higginbotham, William K., Jr., and Falanga,
   Ralph A.: Design and Evaluation of a Turbojet Exhaust Simulator,
   Utilizing a Solid-Propellant Rocket Motor, for Use in Free-Flight
   Aerodynamic Research Models. NACA RM L54I15, 1954.

2. Mason, Homer P., and Gardner, William N.: A Limited Correlation of
   Atmospheric Sounding Data and Turbulence Experienced by Rocket-
   Powered Models. NACA TN 3953, 1957.

3. Gillis, Clarence L., Peck, Robert F., and Vitale, A. James.: Prelim-
   inary Results From a Free-Flight Investigation at Transonic and
   Supersonic Speeds of the Longitudinal Stability and Control Charac-
   teristics of an Airplane Configuration With a Thin Straight Wing of
   Aspect Ratio 3. NACA RM L9K25a, 1950.

4. Mitcham, Grady L., Stevens, Joseph E., and Norris, Harry P.: Aero-
   dynamic Characteristics and Flying Qualities of a Tailless
   Triangular-Wing Airplane Configuration As Obtained From Flights of
   Rocket-Propelled Models at Transonic and Low Supersonic Speeds.
   NACA TN 3753, 1956. (Supersedes NACA RM L9L07.)

5. Peck, Robert F.: Jet Effects on Longitudinal Trim of an Airplane
   Configuration Measured at Mach Numbers Between 1.2 and 1.8.
   NACA RM L54J29a, 1955.

6. Mitcham, Grady L.: A Summary of the Longitudinal and Lateral Stabil-
   ity and Control Characteristics Obtained From Rocket-Model Tests of
   a Swept-Wing Fighter-Type Airplane at Mach Numbers From 0.5 to 1.9.
   NACA RM L56K19, 1957.

7. Englert, Gerald W., Wasserbauer, Joseph F., and Whalen, Paul: Inter-
   action of a Jet and Flat Plate Located in an Airstream. NACA
   RM E55G19, 1955.

8. Spreiter, John R.: The Aerodynamic Forces on Slender Plane- and
   Cruciform-Wing and Body Combinations. NACA Rep. 962, 1950.
   (Supersedes NACA TN's 1897 and 1662.)

9. Nielsen, Jack N., Katzen, Elliott D., and Tang, Kenneth K.: Lift
   and Pitching-Moment Interference Between a Pointed Cylindrical Body
   and Triangular Wings at Various Aspect Ratios at Mach Numbers of
   1.50 and 2.02. NACA TN 3795, 1956. (Supersedes NACA RM A50F06.)

10. Cohen, Doris: Formulas for the Supersonic Loading, Lift, and Drag of
    Flat Swept-Back Wings With Leading Edges Behind the Mach Lines.
    NACA Rep. 1050, 1951.

11. Mirels, Harold, and Haefeli, Rudolph C.: Line-Vortex Theory for Calculation of Supersonic Downwash. NACA Rep. 983, 1950.

12. Vitale, A. James: Effects of Wing Elasticity on the Aerodynamic Characteristics of an Airplane Configuration Having 45° Swept-back Wings As Obtained From Free-Flight Rocket-Model Tests at Transonic Speeds. NACA RM L52L30, 1953.

TABLE I

PHYSICAL CHARACTERISTICS OF THE MODELS

(a) Geometric Characteristics

	Wing	Stabilizer	Fin
Aspect ratio	3.0	3.0	1.5
Sweepback of quarter chord, deg	52.5	52.5	52.5
Taper ratio	0.2	0.2	0.2
Incidence, deg	0	-1.0	0
Dihedral, deg	-5.0	------	------
Area (total), sq ft	4.88	0.78	0.62
Span (total), in.	45.90	18.36	11.61
Root chord, in.	25.50	10.20	12.90
Tip chord, in.	5.10	2.04	2.58
Mean aerodynamic chord, in.	17.57	7.03	8.90
Vertex location, in.:			
Horizontal station	31.36	74.78	76.04
Vertical station	0	5.0	6.0
Fuselage station leading edge of $\bar{c}$ . . .	44.98	80.23	82.93
Spanwise station of $\bar{c}$	8.92	3.57	4.51
NACA airfoil section	65A004	65A006	65A006

(b) Mass characteristics

	Model I		Model II	
	Loaded	Unloaded	Loaded	Unloaded
Center of gravity:				
Horizontal station, in.	49.69	49.49	49.29	49.09
Percent aft leading edge of $\bar{c}$ . . .	26.8	25.7	24.5	23.4
Vertical station	0	0	0	0
Weight, lb	189	169	190	170
Wing loading, lb/sq ft	38.8	34.7	39.0	34.9
Moments of inertia, slug-ft^2:				
I_X, slug-ft^2	0.96	0.94	1.05	0.96
I_Y, slug-ft^2	12.43	12.10	13.29	13.03
I_Z, slug-ft^2	-----	12.32	-----	12.61
Inclination of the				
principal axis, deg	-----	-----	-----	2.5

TABLE II

BODY ORDINATES

[Dimensions are in inches]
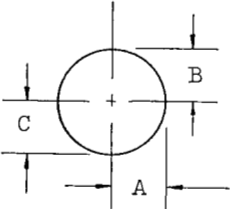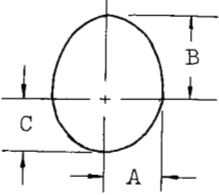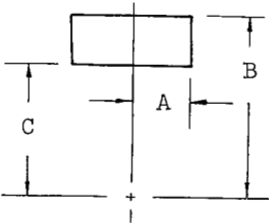
Fuselage station	A	B	C	Cross section
0	0	0	0	
10	1.68	1.68	1.68	
20	2.98	2.98	2.98	Circular
30	3.90	3.90	3.90	
38.12	4.43	4.43	4.43	
40	4.50	4.51	4.49	
50	4.18	4.82	4.39	Two ellipses
60	3.93	5.18	3.90	
70	3.42	5.52	3.02	
77 Jet exit	2.50	5.74	2.20	Fairing from two ellipses ahead of the jet exit to rectangular aft of the jet exit with an abrupt transition occurring at the exit.
80	2.12	5.84	-2.69	
83	2.00	6.00	-3.29	
90	2.00	6.00	-4.70	Rectangular
96.33	2.00	6.00	-6.00	

TABLE III

ACCURACY OF SOME OF THE MEASUREMENTS

[Accuracies are presented for the extreme conditions of
Model II. The accuracies for Model I fall within
these bounds. All values can be either + or -.]

(a) Estimated possible errors in the measured quantities

Quantity	M = 1.12	M = 1.39
W, percent	0.5	0.5
I_Y, percent	2.0	2.0
M, percent	1.29	0.78
q_∞, percent	1.41	1.70
a_Z, g units	0.4	0.4
$\dfrac{da_{Z_{cg}}}{d\alpha}$, percent	2.0	2.0
$\dfrac{da_{Z_{nose}}}{da_{Z_{cg}}}$, percent . . .	2.0	2.0

(b) Calculated probable accuracy of aerodynamic parameters

Increment due to -	$C_{N,trim}$			C_{N_α}		$\dfrac{X_{ac}}{\bar{c}}$	
W	0.0008	0.0009	0.0004	0.0004	0.0003	0.0036	0.0036
I_Y	------	------	------	----------	----------	0.0143	0.0145
q_∞	0.0024	0.0026	0.0012	0.0012	0.0009	----------	----------
a_Z	0.0099	0.0058	0.0058	----------	----------	----------	----------
$\dfrac{da_{Z_{cg}}}{d\alpha}$	------	------	------	0.0016	0.0011	----------	----------
$\dfrac{da_{Z_{nose}}}{da_{Z_{cg}}}$	------	------	------	----------	----------	0.0032	0.0035
Probable error	0.010	0.006	0.006	0.0021	0.0014	0.0151	0.0153
Value of parameter	0.161	0.174	0.0072	0.075	0.057	0.659	0.669
Probable error in percent	6.3	3.5	8.5	2.8	2.5	2.3	2.3
Mach number	1.21	1.39	1.39	1.21	1.39	1.21	1.39
Power	Off	Off	On	Off and on	Off and on	Off and on	Off and on

Front view

Side view
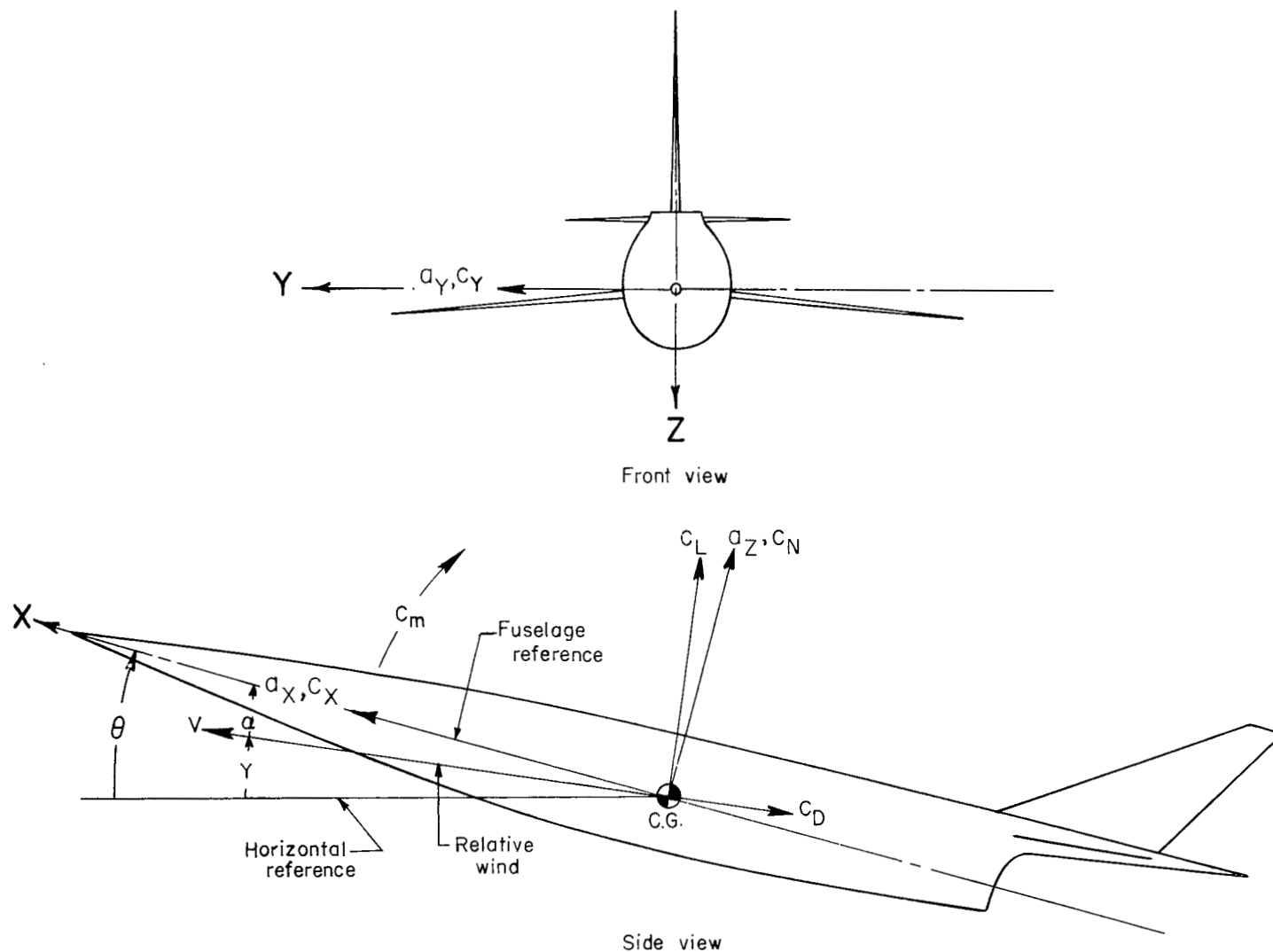
Figure 1.- Body-axis system used in the analysis. Positive directions, forces, and moments are shown by arrows.
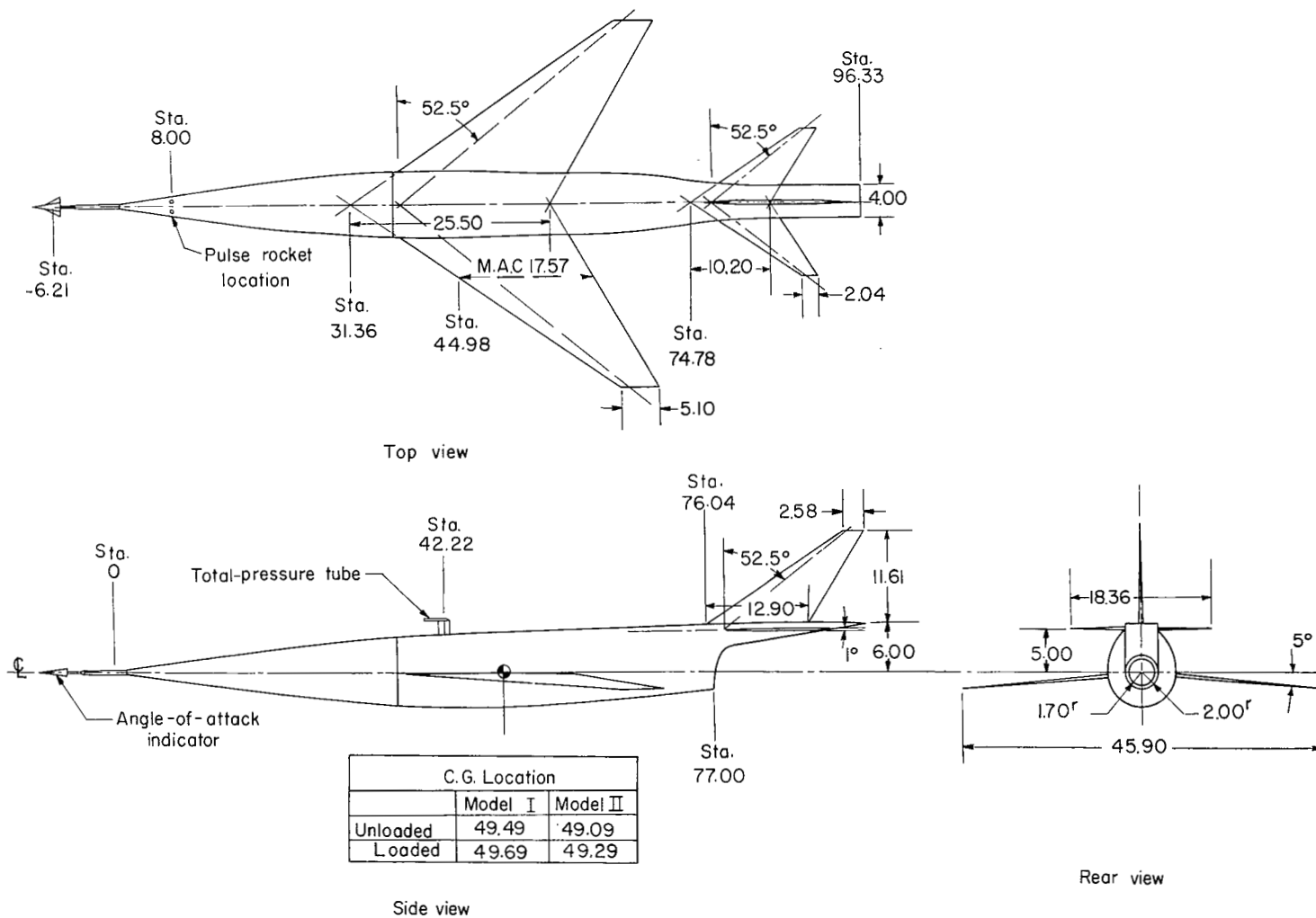
(a) Three-view drawing.

Figure 2.- Model description.
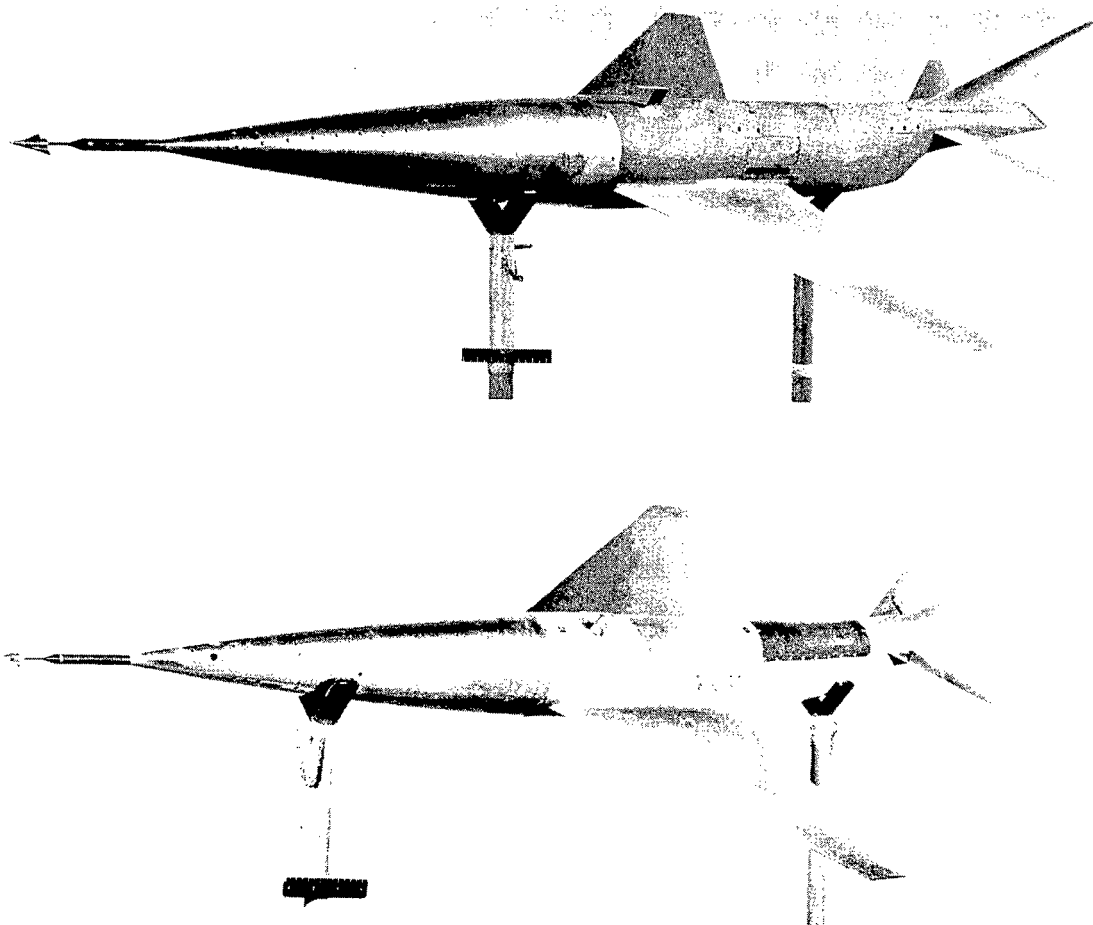
(b) Models I and II.　　　　L-57-1615

Figure 2.- Continued.
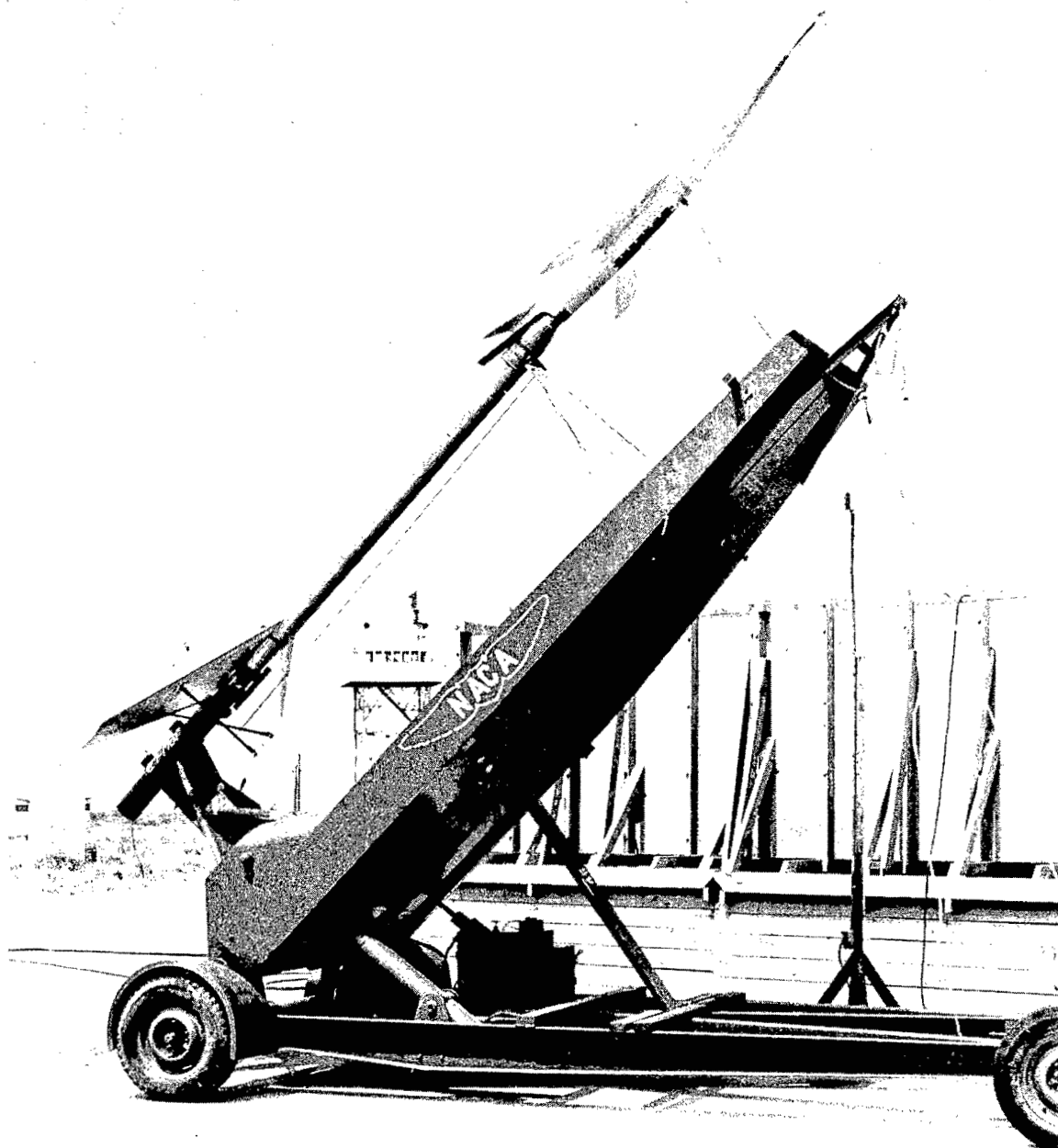
(c) Model on launcher.   L-90106

Figure 2.- Concluded.
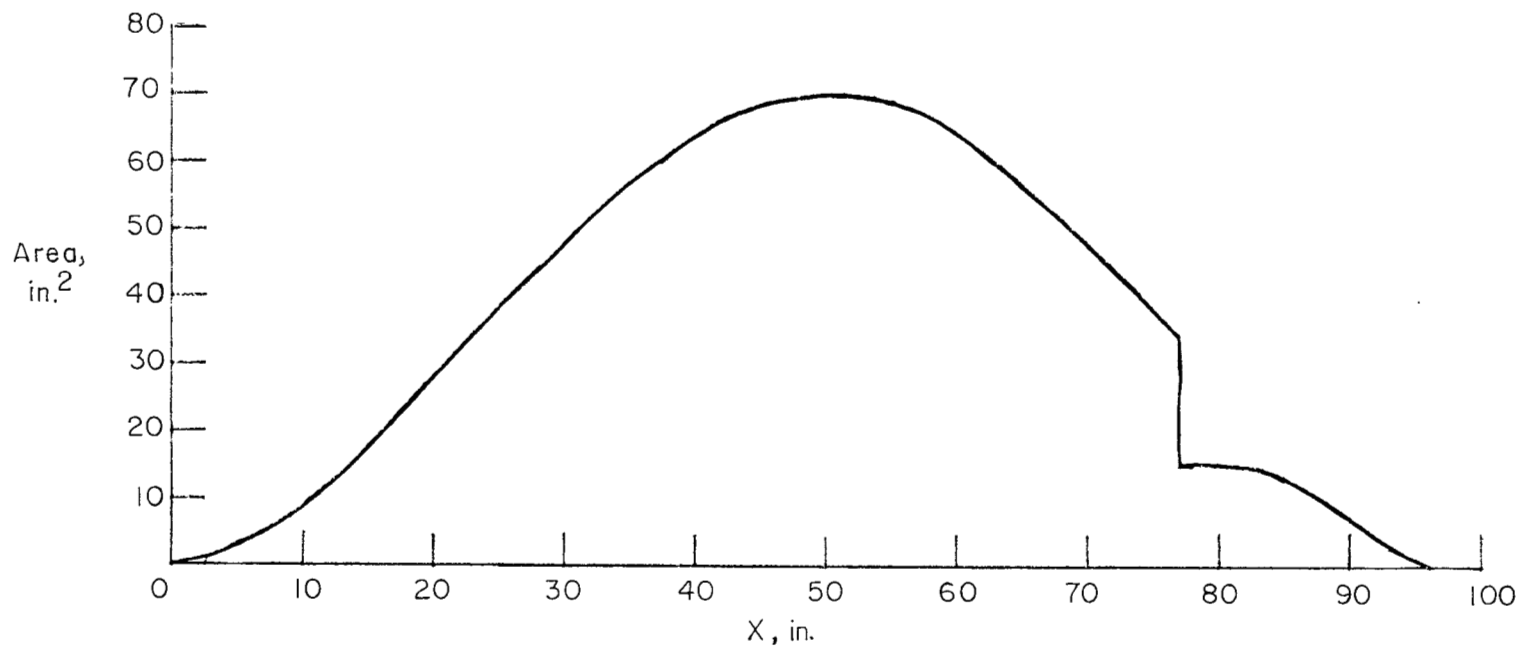
Figure 3.- Normal area distribution.

Rocket chamber diameter, 5.00 in.

Diameter, 3.415 in
Jet exit { area 9.15 sq in.

Booster adapter catch.

Spacer

Igniter

Cordite propellant

Nozzle
13 Throats
area 1.953 sq in.
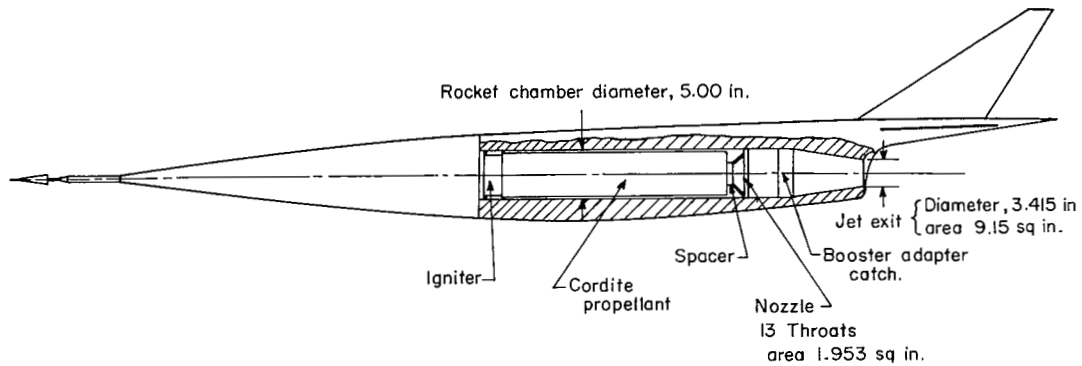
Jet Operating Characteristics Obtained From
A Static Ground Firing

Total temperature of the jet, 3,680° R
Velocity of the jet, 2,810 ft/sec
Weight flow ratio, 5.26 lb/sec, average
Thrust, 741 lb
Jet total pressure, 81.8 lb/sq in. abs
Jet static pressure, 45.6 lb/sq in. abs
Ratio of specific heats, 1.24

(a) Drawing and operating characteristics of the turbojet simulator.
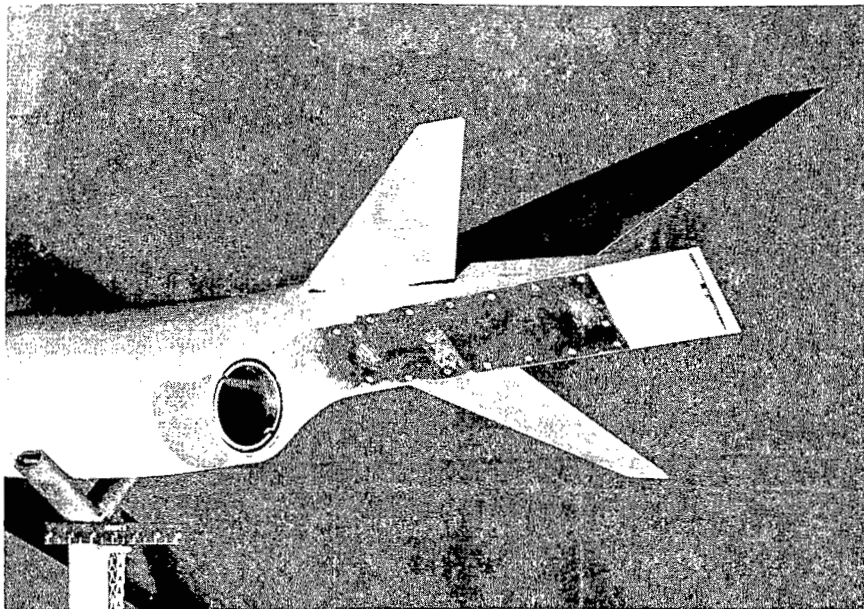
(b) Photograph of jet exit.   L-89721

Figure 4.- Simulator description.
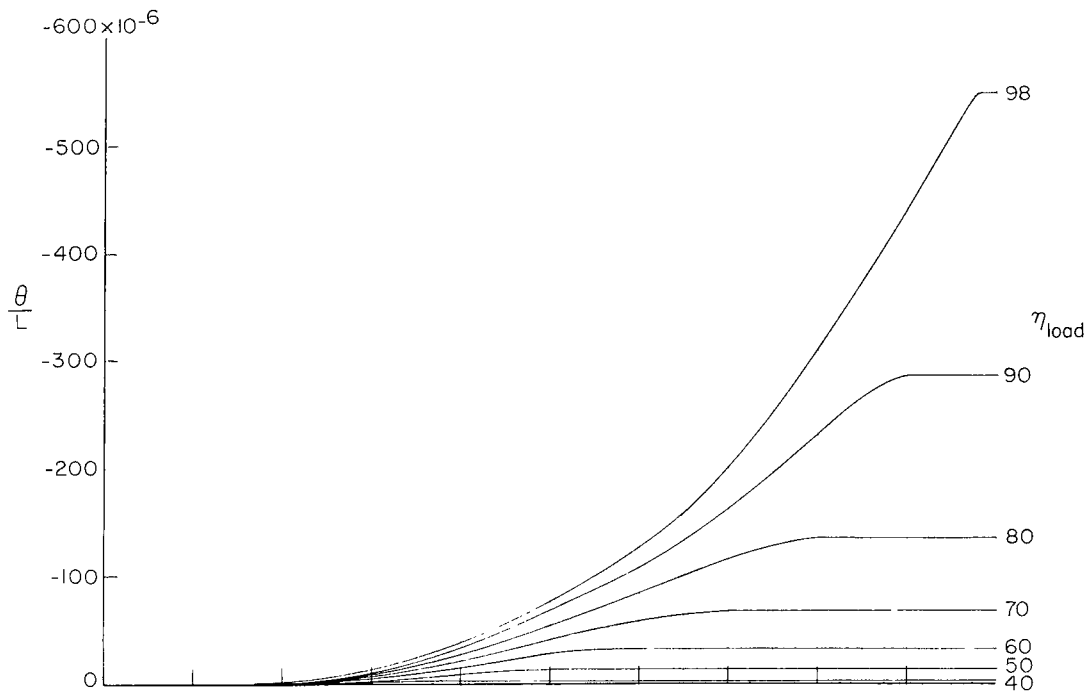
(a) Wing 50 percent chord loading.
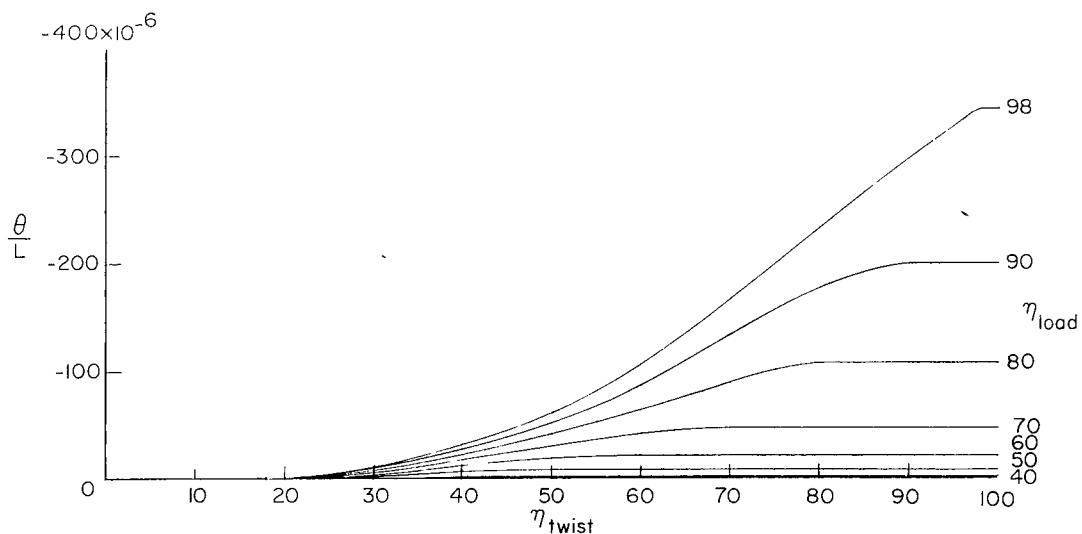
(b) Wing 25 percent chord loading.

Figure 5.- Influence coefficients of twist in the free-stream direction
per unit load applied at various stations along the span.
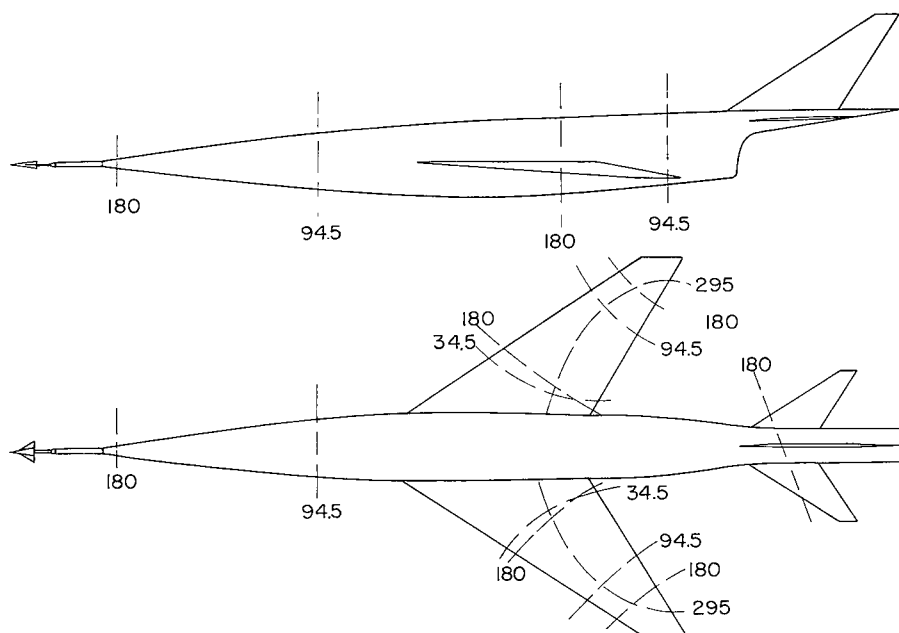
Model I
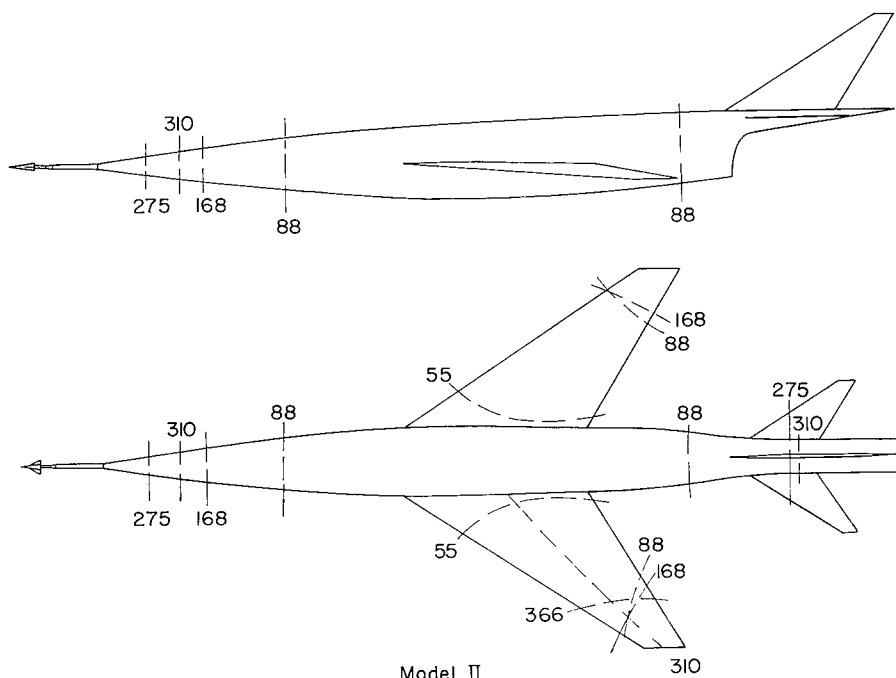
Model II

Figure 6.- Nodal lines and resonant frequencies.
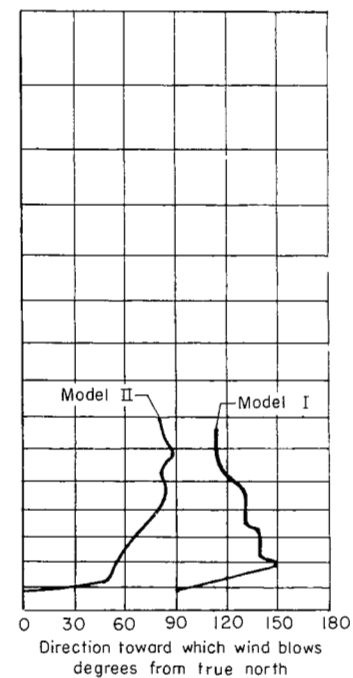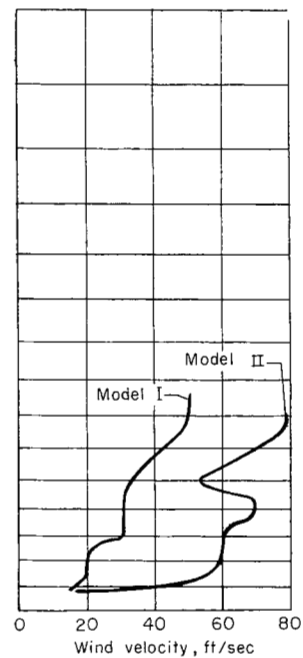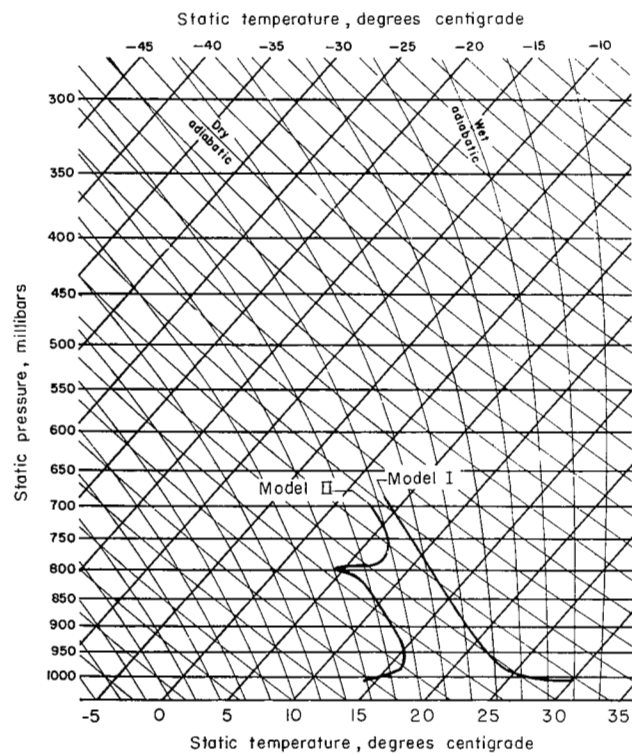
Figure 7.- Atmospheric conditions existing during the test.
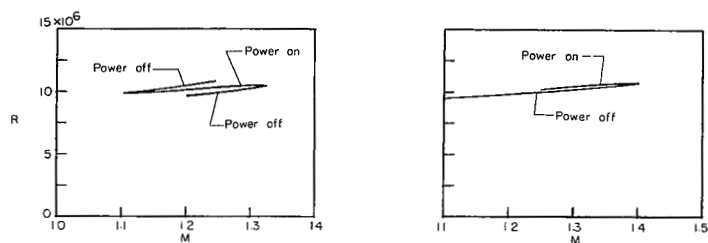
(a) Reynolds number.
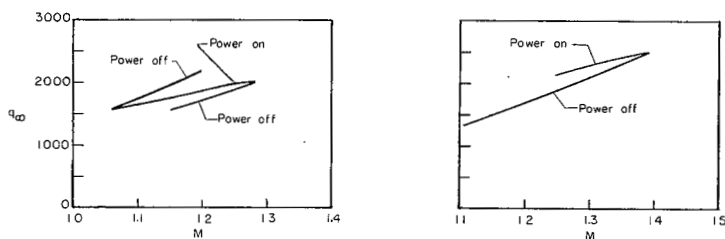
(b) Dynamic pressure.
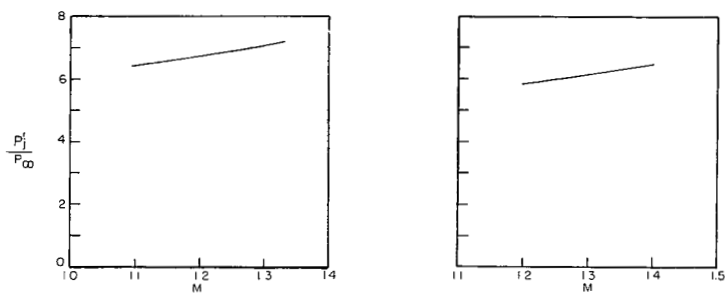
(c) Estimated jet total pressure ratio.
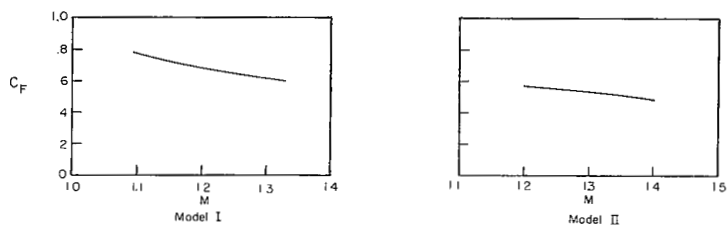
(d) Estimated thrust coefficient.

Figure 8.- Summary of test conditions.
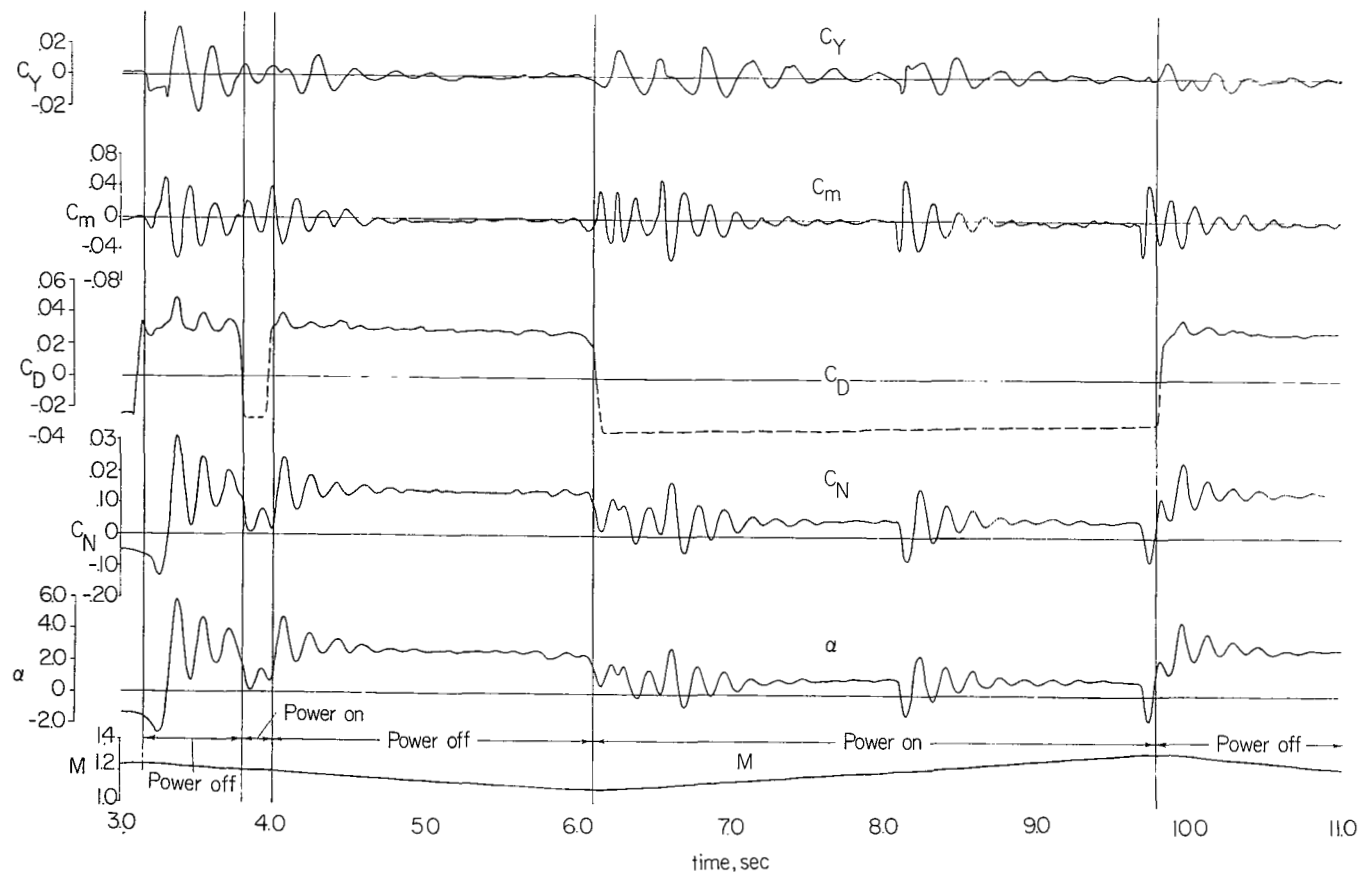
(a) Model I.

Figure 9.- Partial time history.
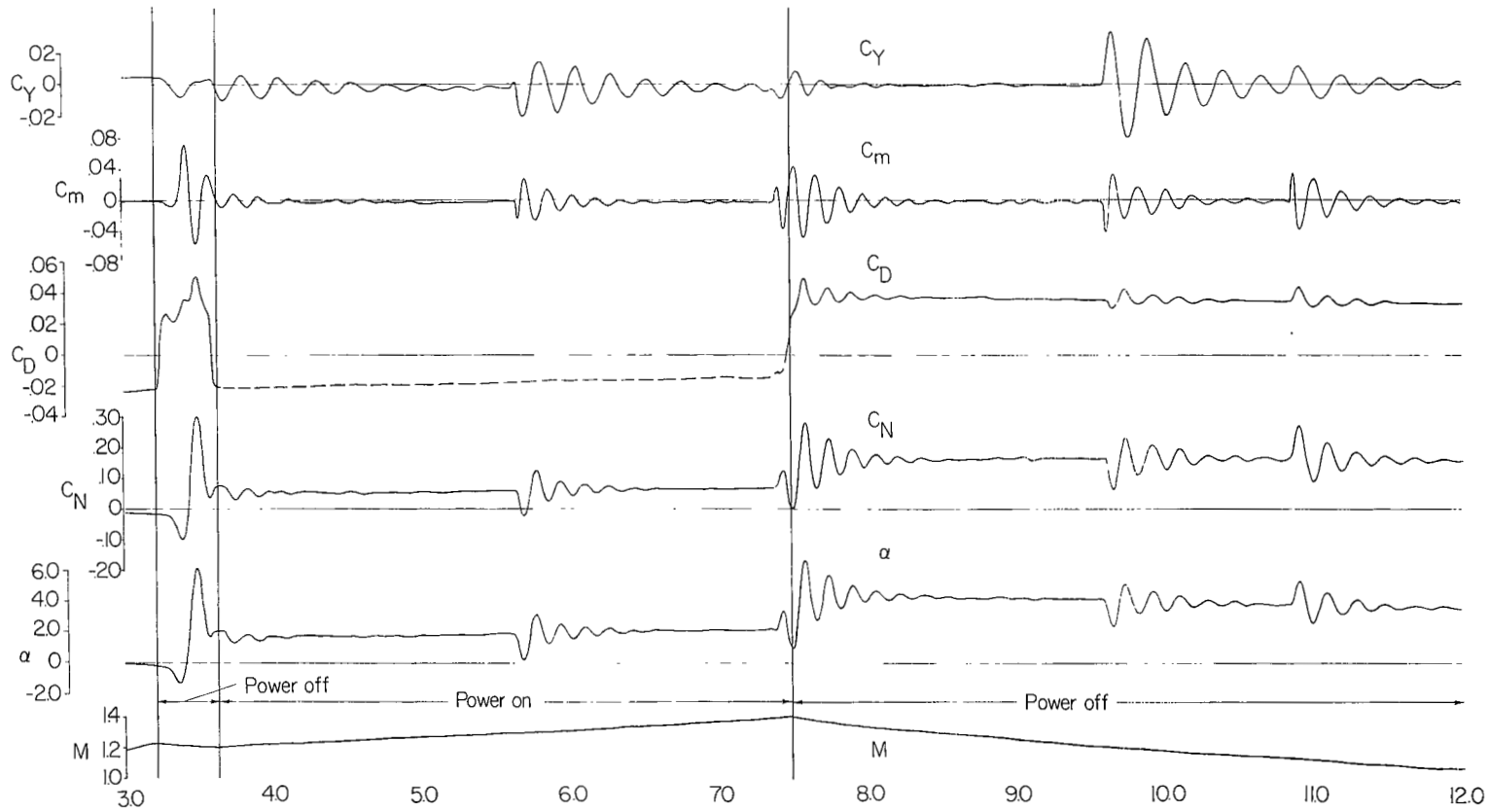
(b) Model II.

Figure 9.- Concluded.
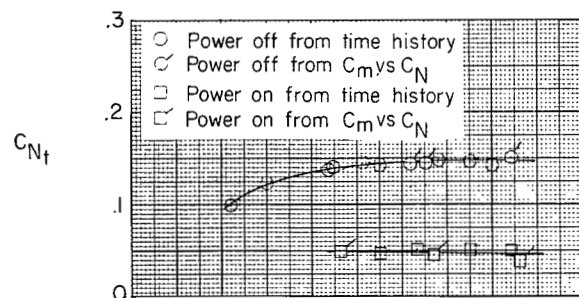
(a) Trim lift coefficient vs Mach number, model I
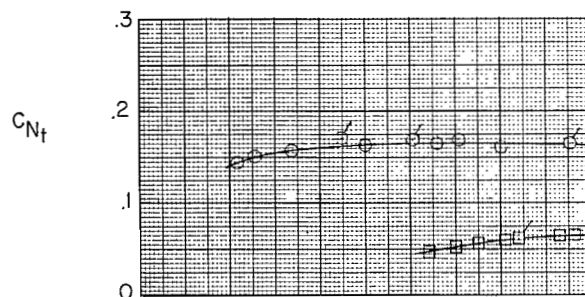
(b) Trim lift coefficient vs Mach number, model II
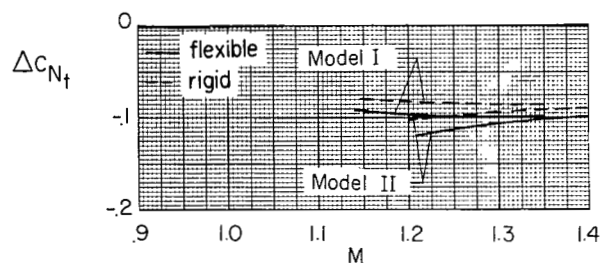
(c) Increment in C_{N_t} due to power vs Mach number
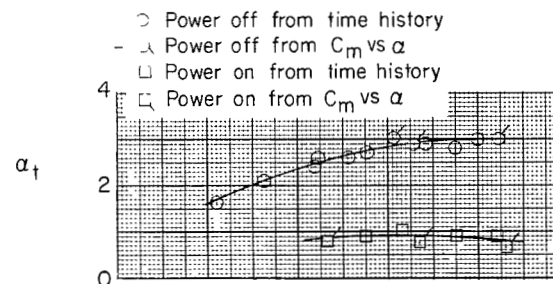
(d) Trim angle of attack vs Mach number, model I
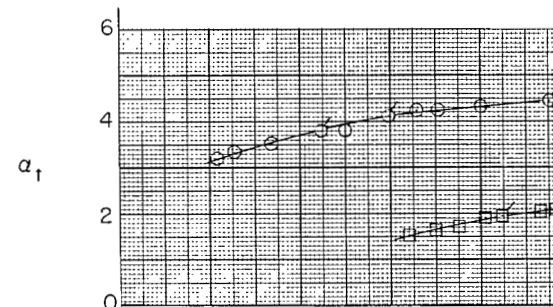
(e) Trim angle of attack vs Mach number, model II
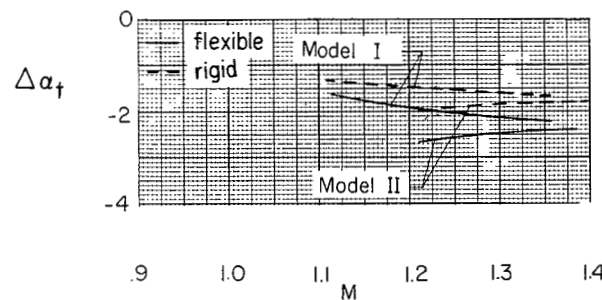
(f) Increment in α_t due to power vs Mach number

Figure 10.- Trim characteristics.

CONFIDENTIAL

C_N
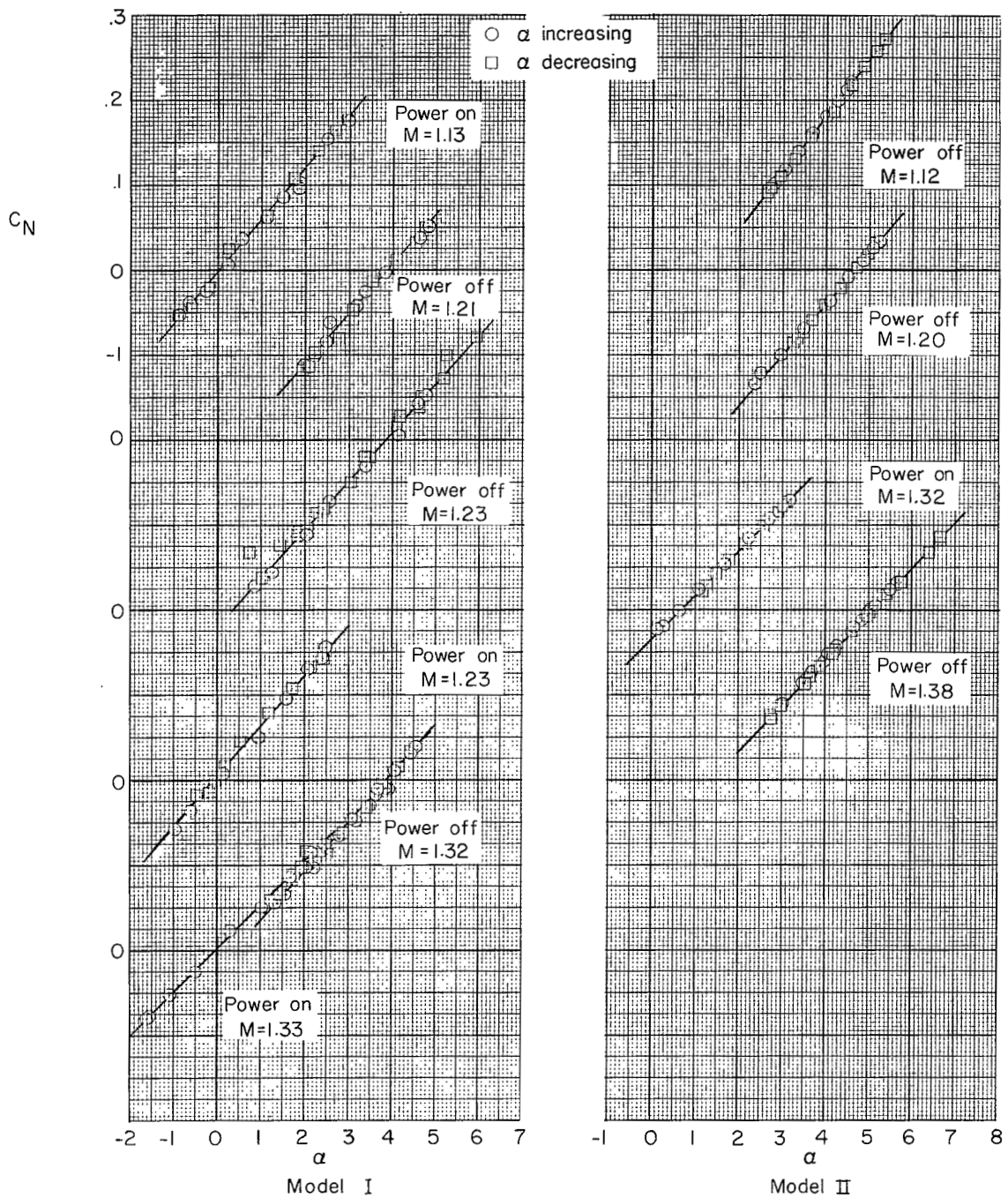
Figure 11.- Basic lift data.
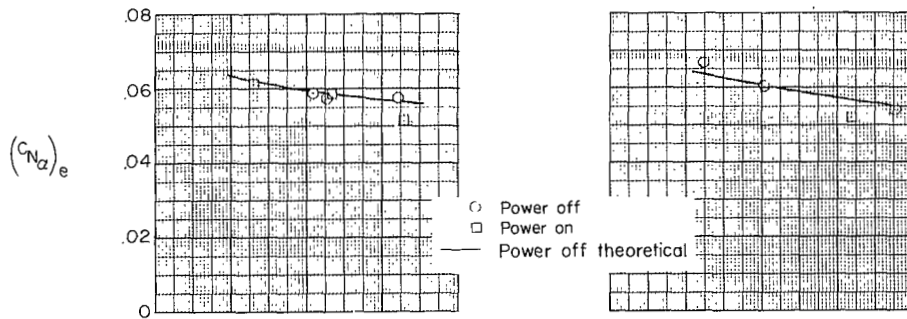
(a) Flexible lift-curve slope plotted against Mach number.
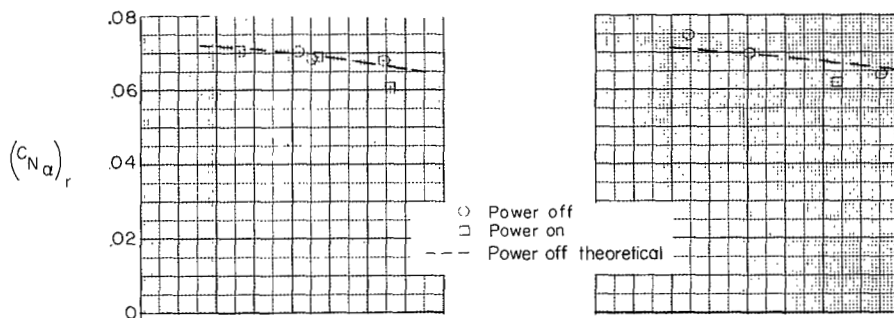
(b) Rigid lift-curve slope plotted against Mach number.
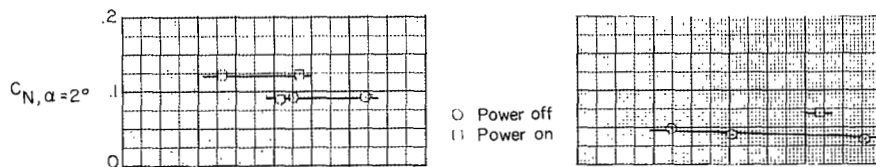
(c) Lift coefficient at constant α plotted against Mach number.
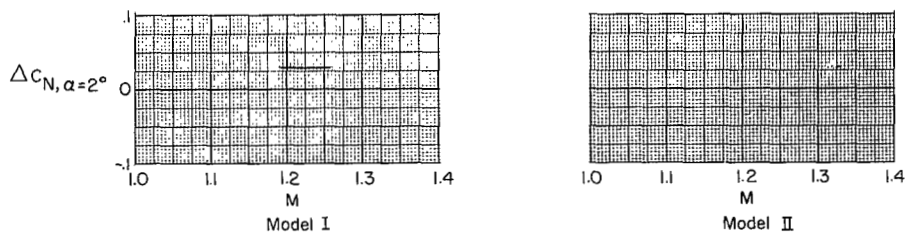
(d) Increment in $C_{N,\alpha=2^\circ}$ due to power plotted against Mach number.

Figure 12.- Lift summary.

CONFIDENTIAL
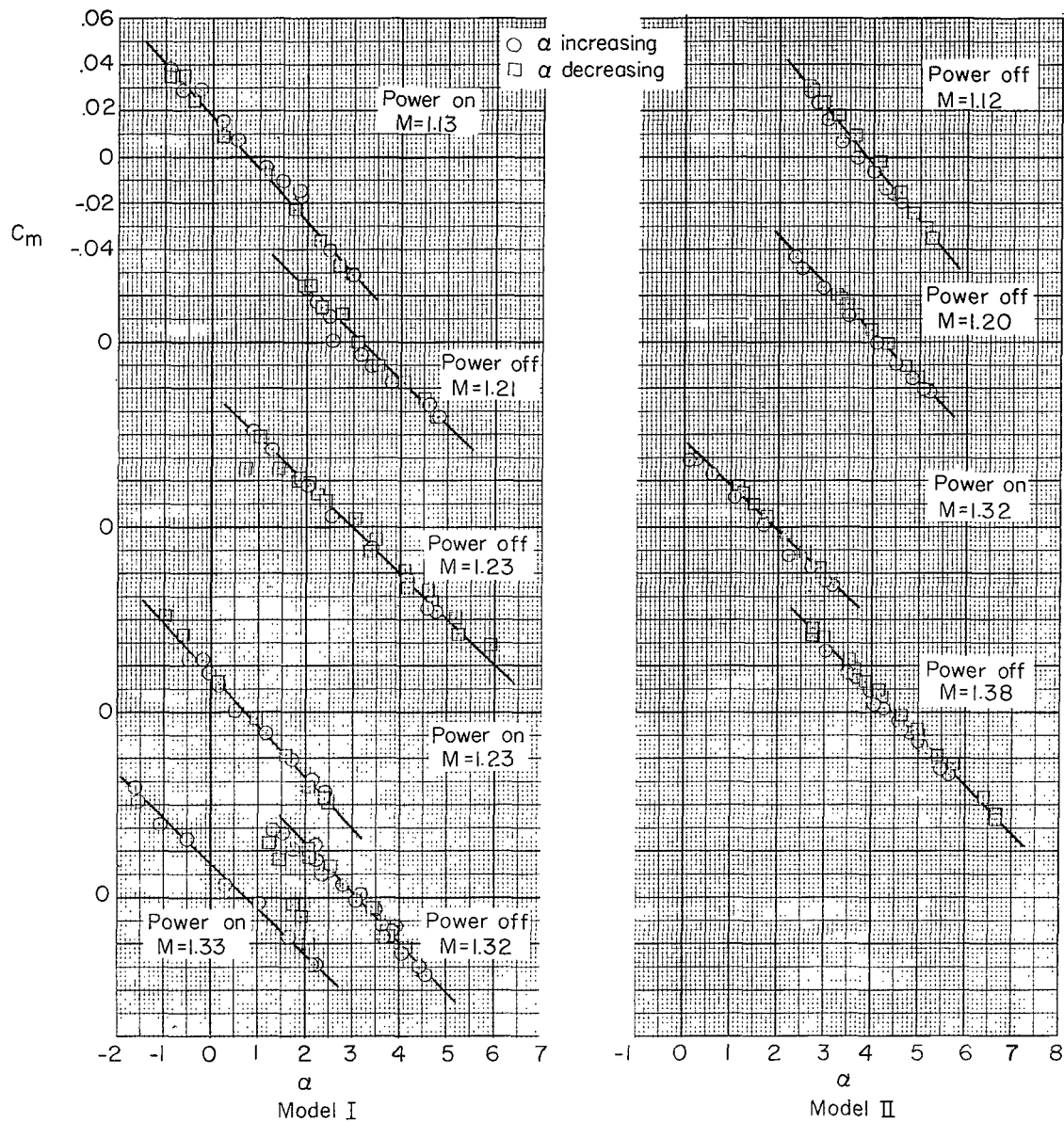
Figure 13.- Basic pitching-moment data.
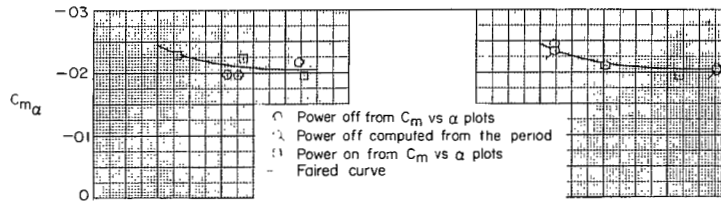
(a) Static stability parameter $\dfrac{dC_m}{d\alpha}$ plotted against Mach number.
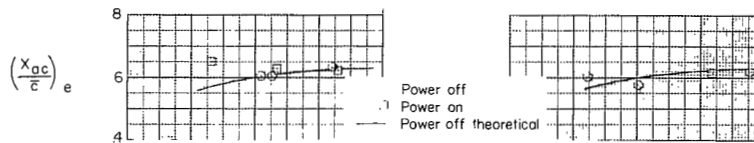
(b) Elastic aerodynamic-center location plotted against Mach number.
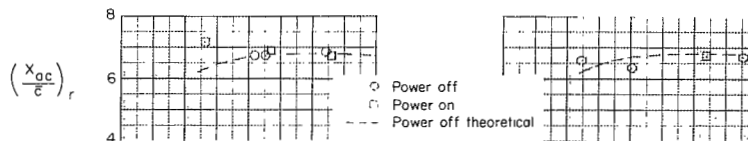
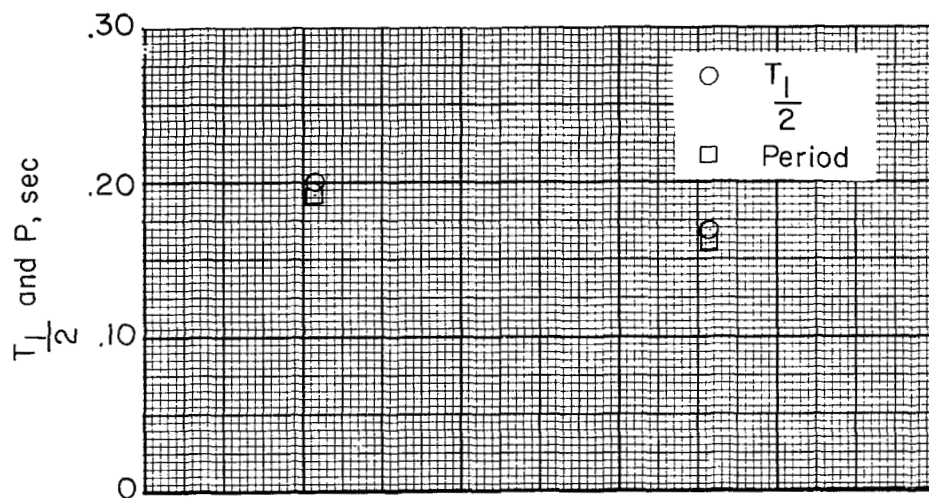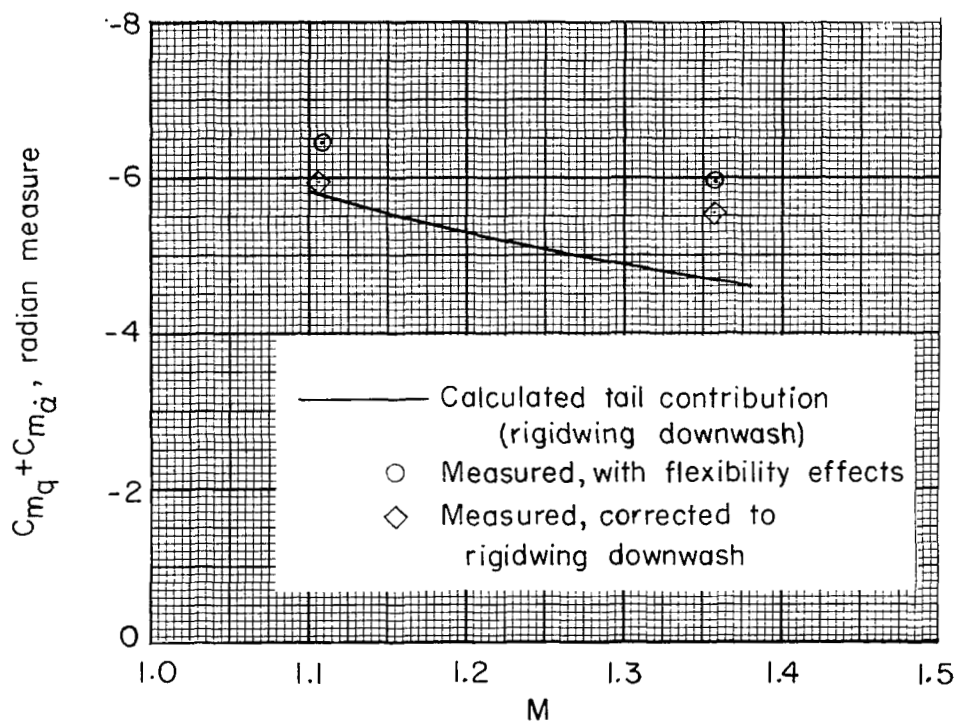(c) Rigid aerodynamic-center location plotted against Mach number.
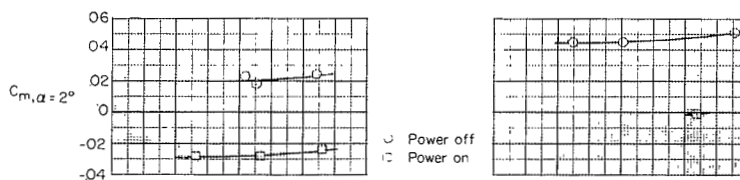
(d) Pitching-moment coefficient at constant angle of attack.
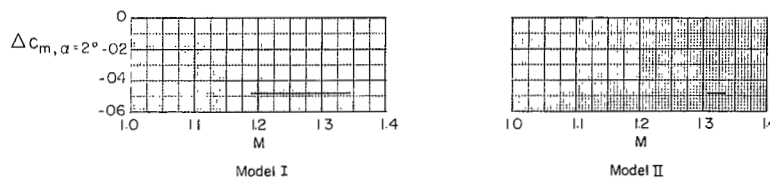
(e) Increment in $C_{m,\alpha=2^\circ}$ due to power vs Mach number.

Figure 14.- Static stability summary.

(a) $T_{1/2}$ and P.

(b) Longitudinal rotary damping.
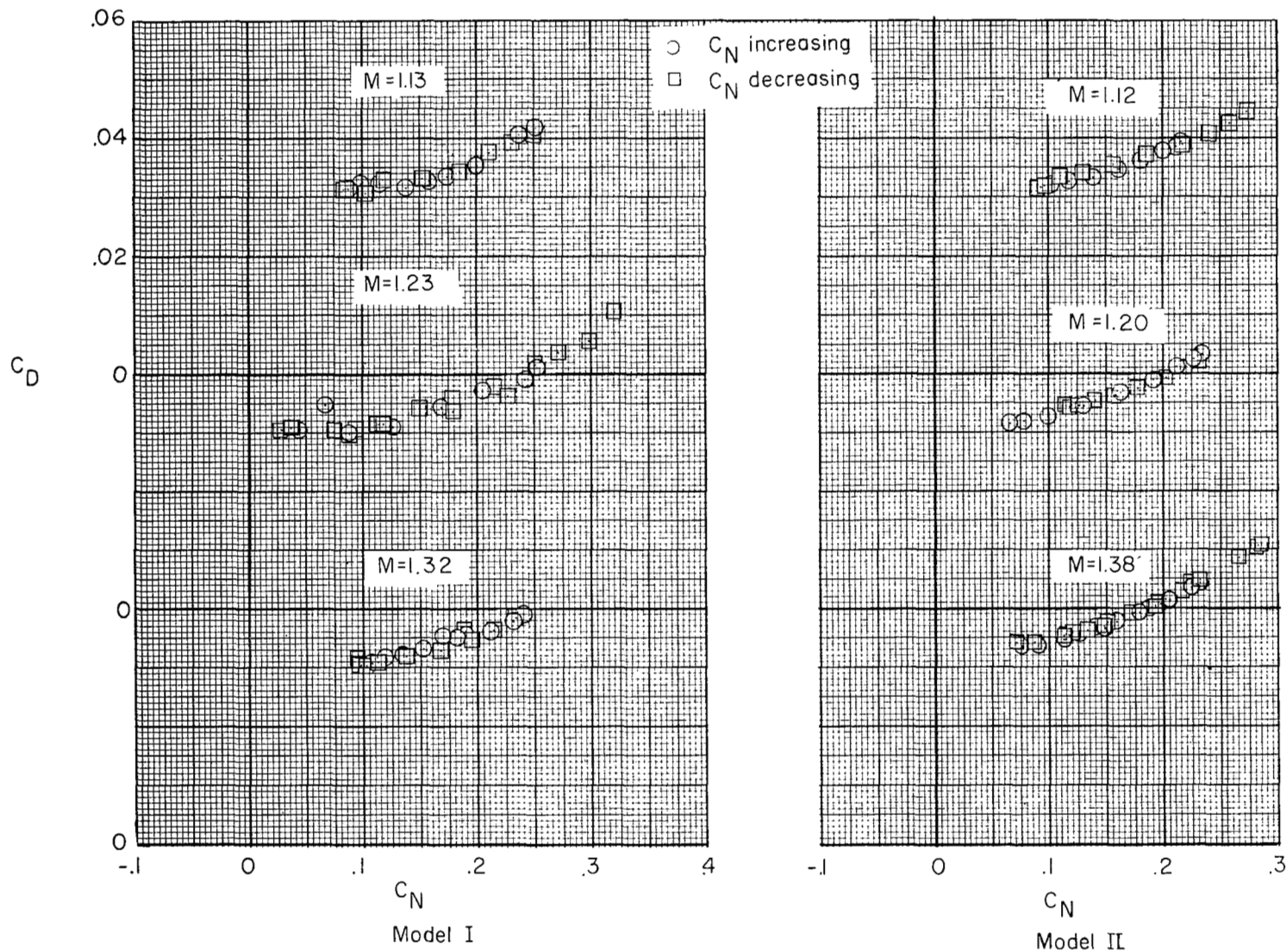
Figure 15.- Power-off longitudinal-dynamic-stability data from model II.

Figure 16.- Basic power-off drag data.